Tuning the electronic structure of d^0 perovskite oxides by combining distortive modes

Dario V. Cirlincione and Robert F. Berger*
Department of Chemistry, Western Washington University, Bellingham 98225, Washington, USA

(Received 20 October 2020; revised 29 December 2020; accepted 7 January 2021; published 20 January 2021)

Transition metal oxides in the d^0 perovskite class, defined broadly to include WO_3, have shown promise as light absorbers for photocatalytic applications. These compounds are highly tunable in their composition and atomic structure, and consequently, in their electronic structure and properties. Through the lens of atomic orbital interactions and density functional theory calculations, the present work explores how and why certain structural distortions tune the band gaps and band edges of WO_3 and d^0 perovskite oxides. It is determined that, because an individual distortive mode (e.g., polar distortion along or octahedral rotation around a cubic perovskite axis) changes the character of only some band-edge orbitals, combinations of distortive modes may tune band gaps much more significantly than the sum of individual modes. The implications of this tunability are discussed for WO_3 as a photocatalyst, and for d^0 perovskite oxides more generally.

DOI: 10.1103/PhysRevB.103.045127

I. INTRODUCTION

Since the identification of $SrTiO_3$ as a light-absorbing material that facilitates the splitting of water into its elements [1,2], compounds in the d^0 perovskite oxide family have been developed for photocatalytic processes including water splitting, the oxidation of organic molecules, and the reduction of CO_2 [3–8]. These perovskite oxides have the general formula ABO_3, in which the A site is typically occupied by alkali or alkaline earth cations, and the B site is occupied by transition metal cations.

In these compounds, when a solar photon excites an electron from valence band (primarily oxygen $2p$ character) to conduction band (primarily B-site d character), the excited electron and hole can then drive the redox half-reactions of the process of interest. An effective photocatalyst must have band edges that lie outside the relevant redox potentials, and ideally, a band gap small enough to absorb a significant fraction of solar photons. Often, d^0 perovskites such as $SrTiO_3$ ($E_g = 3.2$ eV [9]) have relatively wide band gaps that limit their ability to absorb sunlight.

It is therefore desirable to devise and understand routes to tune the band gaps and band edges of these compounds. Due to their shallow structural energy landscapes, perovskites are particularly amenable to many modes of structural modification, which in turn can tune their electronic structure. These degrees of structural modification include changes in elemental identity, temperature-controlled geometric distortions [10,11], isotropic or biaxial strain [12,13], the growth of ordered superstructures [14,15], and the engineering of various types of defects [16,17]. All of these degrees of structural tunability affect one another, and their effects on the electronic structure are intertwined. The complex structure-property relationships in this family of compounds present a conceptual challenge, but also exciting opportunities to tailor these materials for photocatalysis. Computation allows us to examine and rationalize the effects of each tunable parameter from the viewpoint of interactions of atomic orbitals and leverage the parameters to productively tune the band edges of these materials. Examples of this type of computational analysis have been seen previously for perovskite oxides [18–21].

In the present work, we focus many of our calculations on WO_3 as a representative of d^0 perovskites. This may seem an odd choice, as the A site of WO_3 is unoccupied, and it is therefore not traditionally considered a perovskite. However, WO_3 is electronically analogous to other d^0 perovskites, and proves to be an interesting case study for several reasons. With changing temperature, WO_3 exhibits a complex series of phase transitions with both B-site translations and octahedral rotations [22–25], providing unique opportunities to harness electronic tunability. Its optical and conductive properties, as well as the amplitudes of its distortions, are also tunable via the intercalation of alkali metals over wide compositional ranges (e.g., Na_xWO_3) [26–28]. Like its perovskite oxide relatives, WO_3 has been studied for its photocatalytic properties, particularly as a photoanode for water splitting [29–32]. While its conduction band edge is too low for hydrogen evolution, its high-energy valence band edge and its band gap that is smaller than many perovskite oxides make WO_3 an active photocatalyst for oxygen evolution, and promising in schemes for solar water splitting [3]. Based on optical band-gap measurements of WO_3 films, a complex story emerges in which the room-temperature band gap varies from approximately 2.8–3.2 eV depending on growth conditions [33,34], with the low end of that range representing stoichiometric WO_3 and the high end having excess oxygen [35,36].

The structural and electronic properties of WO_3 have been the subject of numerous DFT-based studies. Past work has focused on precise calculations of the band structure and absorption spectrum using many-body methods [33,37,38], the energetics of structural distortions and their dependence

*Robert.Berger@wwu.edu

on computational method [39,40], the use of doping and vacancies at the oxygen and tungsten sites to tune structural and electronic properties [41–44], and the effects of cation intercalation at the vacant A site [45–48]. Like the present work, there have also been investigations of the relationships between the structural features and distortions of WO_3 and its electronic structure [49,50].

In this paper, we aim to articulate a unifying framework for viewing WO_3 and d^0 perovskite oxide band gaps and band-edge orbitals, and the ways that various degrees of structural flexibility (composition, distortion, and strain) conspire to tune them. We then use these ideas to discuss the opportunities and challenges in optimizing WO_3 and d^0 perovskites for photocatalysis. Particularly relevant to the present discussion, the work of de Wijs and coworkers on WO_3 [50] and the work of Berger and coworkers on epitaxially strained $SrTiO_3$ [19] identify some of the specific orbital interactions (e.g., the mixing of band-edge states that accompanies ferroelectric distortion) that can tune the near-gap electronic structure of perovskites. Our work builds upon these ideas and more deeply explores the surprising effects of *combining* multiple distortive modes. We find that combinations of distortions often have synergistic effects, understandable based on arguments of crystal orbital symmetry and character, that tune band gaps and band edges more than one might expect based on the individual distortive modes.

II. COMPUTATIONAL METHODS

Crystal structures are optimized within density functional theory (DFT) using the VASP package [51–54] and projector augmented wave method (PAW) potentials [55]. Calculations employ three different classes of density functionals: the local density approximation (LDA), the Perdew—Burke—Ernzerhof (PBE) functional [56] (a generalized gradient approximation), and the Heyd—Scuseria—Ernzerhof 06 (HSE06) hybrid functional [57]. Structural geometries are optimized within LDA and PBE, while HSE06 calculations use the optimized PBE geometries. Previous work on the relationships between the atomic and electronic structure of WO_3 has often used hybrid functionals [39,40]. However, while LDA and PBE are known to underestimate band gaps relative to experiments, they have been demonstrated to accurately capture the energetics of structural distortions and the trends in band gap for this particular class of compounds [19,58]. So too in the present work, LDA and PBE produce band gap trends very similar to HSE06 for this class of compounds, despite their lower computational cost. For these reasons, we primarily describe LDA results in this paper, also presenting PBE and HSE06 results when necessary to demonstrate that our conclusions are largely independent of the choice of functional.

The plane-wave basis set cutoff is 500 eV for all compounds. Unit cells containing one perovskite formula unit are treated with a Γ-centered $6 \times 6 \times 6$ k-point mesh, while proportionally fewer k-points are used for structures requiring larger unit cells. Biaxial strain is modeled by fixing in-plane lattice parameters while allowing the perpendicular axis and atomic positions to relax. In cases where the band-edge energies of WO_3 are reported, they are referenced to the flat semi-core tungsten 5s band, and shifted such that the conduction band minimum of cubic WO_3 is defined as zero energy.

A variety of combinations of elements are computed with the forms $A^{2+}B^{4+}O_3^{2-}$ (A = Ca, Sr, Ba; B = Ti, Zr, Hf), $A^{+}B^{5+}O_3^{2-}$ (A = Li, Na, K; B = Nb, Ta), or $B^{6+}O_3^{2-}$ (B = W). WO_3, while not always classified as a "perovskite," is essentially a perovskite with a vacant A site, and is electronically analogous to other d^0 perovskites. For all elements, atomic potentials are chosen such that as many electrons as possible are treated as valence (details in the Supplemental Material [59]).

III. RESULTS AND DISCUSSION

A. Cubic compounds

To provide a baseline for subsequent results, we begin by describing the electronic band structure of cubic d^0 perovskite oxide compounds with a variety of compositions. The prototypical cubic $Pm\bar{3}m$ phase exists at room temperature for several perovskites (e.g., $SrTiO_3$, $BaZrO_3$, and $NaNbO_3$) and for many more at higher temperatures. For the 16 combinations of elements computed in this paper, the shapes of the valence and conduction bands and the character of the band-edge orbitals are qualitatively similar [examples shown in Figs. 1(a) to 1(c)]. In all cases, the cubic band gap is indirect, with a threefold-degenerate valence band maximum (VBM) at k-point $R = (\frac{1}{2}, \frac{1}{2}, \frac{1}{2})$ and a threefold-degenerate conduction band minimum (CBM) at k-point $\Gamma = (0, 0, 0)$. As shown in the WO_3 band-edge orbitals in Fig. 1(a), the VBM are primarily antibonding combinations of oxygen 2p orbitals, while the CBM are primarily nonbonding combinations of the t_{2g} set of B-site d orbitals. Neither band edge has significant A-site character, which explains why the band structure stays qualitatively the same even when the A site is vacant in WO_3. In subsequent sections of this paper, we will explore how these cubic crystal orbitals mix and their degeneracies break as the perovskite structure distorts to lower symmetries.

For the test set of 16 cubic compounds, computed band gaps are compared for LDA and HSE06 hybrid functional calculations [Fig. 1(d)]. While LDA calculations underestimate band gaps as expected, LDA band gaps correlate strongly with the more quantitatively reliable HSE06 gaps. (Further comparisons in the Supplemental Material [59] show that calculations using the PBE functional, a generalized gradient approximation, also produce similar trends.) This suggests that LDA calculations are sufficient to highlight trends in band gap with changing composition. It is also worth noting that, consistent with the B-site character of the CBM, the band gaps of d^0 perovskite oxides depend primarily on the identity of the B-site element. For a given B-site element, band gaps depend more finely on the identity of the A-site element—not because it changes the character of the band-edge orbitals, but because it affects the unit cell size.

B. Common perovskite distortions

While the cubic compounds described in the previous section provide a conceptual baseline, most perovskites adopt series of temperature-controlled structural distortions that tune the electronic structure. These distortions typically come

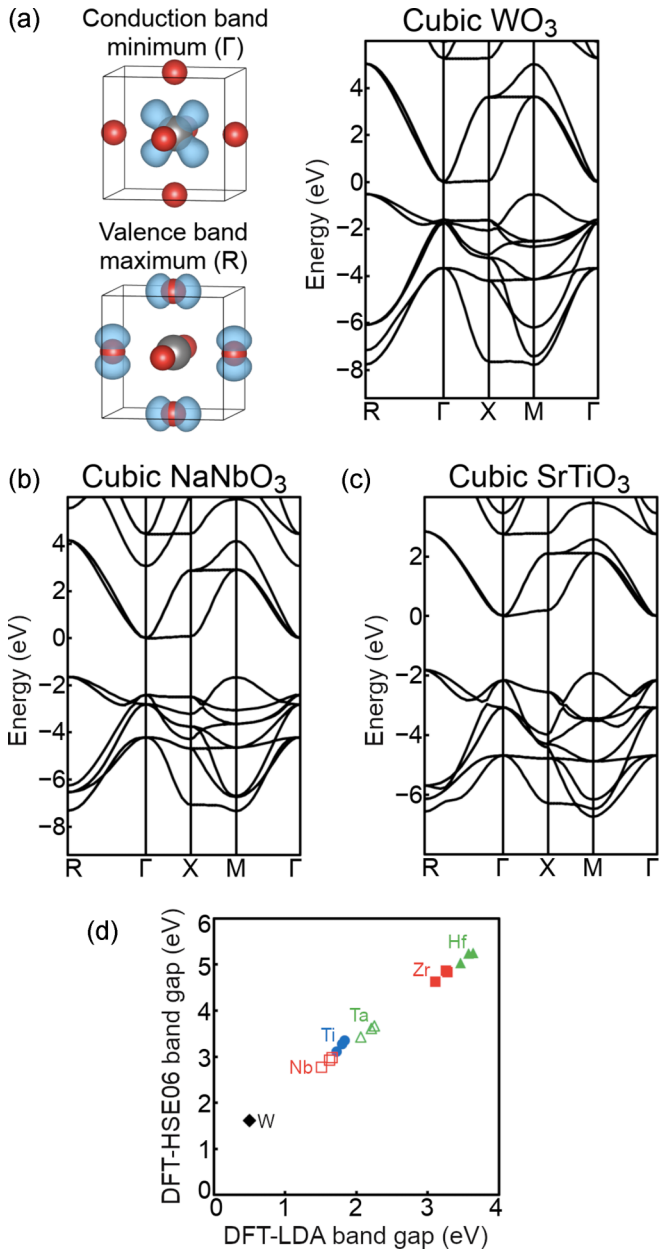

FIG. 1. Cubic band structures of (a) WO_3, (b) $NaNbO_3$, and (c) $SrTiO_3$, with the conduction band minimum of each compound defined as zero energy. Electron densities associated with the band-edge orbitals are shown for WO_3. (d) For the test set of 16 compounds, DFT-computed band gaps are compared for the LDA and HSE06 functionals, grouped by the identity of the B-site element.

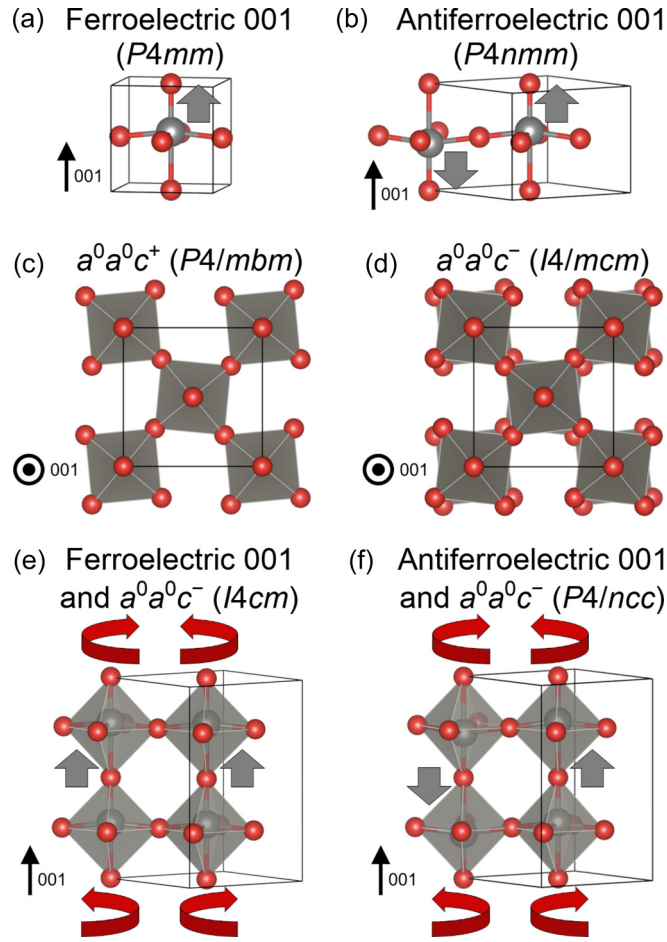

FIG. 2. Common perovskite distortive modes illustrated for WO_3, with gray and red arrows indicating the movements of tungsten and oxide ions, respectively. Distorted phases include (a) ferroelectric and (b) antiferroelectric phases in which B-site cations shift in the 001 direction (along with small movements of the oxide anions), patterns of octahedral rotation described by (c) $a^0a^0c^+$ and (d) $a^0a^0c^-$ in Glazer notation [62] and combinations of $a^0a^0c^-$ rotation with (e) ferroelectric and (f) antiferroelectric distortion. Images of crystal structures throughout this work are made using the software VESTA [64].

in two classes: modes in which B-site cations shift off-center in their octahedral oxide cages, and modes in which B–O octahedra collectively rotate. In general, the types and amplitudes of distortions present for a given set of elements are governed by how the sizes of the ions fit together. For almost a century, the Goldschmidt tolerance factor [60] (defined as $t = \frac{r_A + r_O}{\sqrt{2}(r_B + r_O)}$) and modern updates to it [61] have been used as rough predictors of perovskite stability and distortion. When t is somewhat greater than 1 (i.e., large A site and small B site), distortions typically involve movement of the B-site cations relative to their neighbors. When t is somewhat less than 1 (i.e., small A site and large B site), distortions typically involve octahedral rotations. The amplitudes of structural distortions also depend on tolerance factor and can be further tuned by isotropic or epitaxial strain.

Phases with several of these distortive modes are illustrated in Fig. 2 for WO_3, with translations and rotations of the ions along and around an O–B–O bond axis defined as the 001 direction. In the polar ferroelectric [*P4mm*, Fig. 2(a)] and nonpolar antiferroelectric [*P4nmm*, Fig. 2(b)] phases, B-site cations and oxide anions shift relative to each other, resulting in B-site cations that lie off-center within oxide octahedra. The phases described by $a^0a^0c^+$ [*P4/mbm*, Fig. 2(c)] and $a^0a^0c^-$ [*I4/mcm*, Fig. 2(d)] in Glazer notation [62] feature B–O octahedral rotations. The last two tetragonal phases are representative of the ways that ferroelectric [*I4cm*, Fig. 2(e)] or antiferroelectric [*P4/ncc*, Fig. 2(f)] modes can combine with $a^0a^0c^-$ rotations. The structure in Fig. 2(f) is a phase of

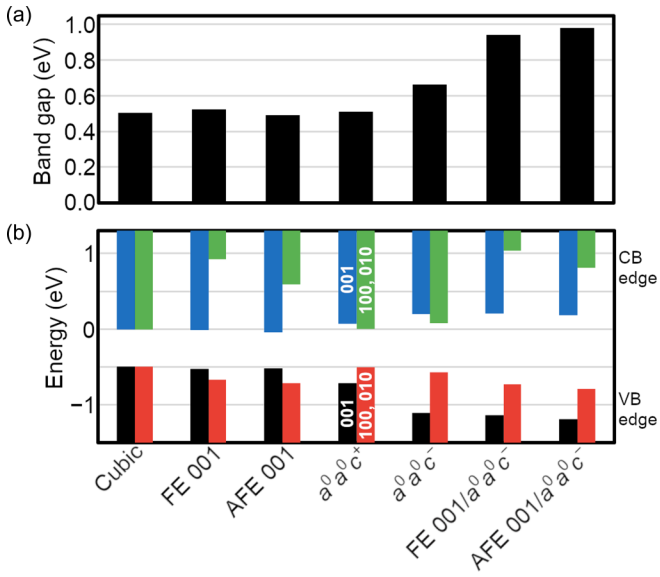

FIG. 3. (a) DFT-LDA-computed band gaps of various phases of WO_3. (b) Energies of the band-edge orbitals of cubic WO_3 are traced through the lower-symmetry phases of WO_3. Orbitals are separated between those lying in the 001 planes (blue and black bars) and those lying in the 100 and 010 planes (green and red bars). Band-edge energies are referenced to the flat tungsten 5*s* bands, and shifted such that the conduction band minimum of cubic WO_3 is defined as zero energy.

WO_3 that exists between approximately 700° C and 900° C, [22–25] while the structure in Fig. 2(e) is its close energetic competitor that is preferred in compounds such as $SrTiO_3$ under compressive epitaxial strain [19,63]. The computed coordinates of these and other WO_3 phases are provided in the Supplemental Material [59].

Using the cubic band-edge orbitals in the previous section as a starting point, we are now ready to focus on how and why structural distortions tune band gaps and band edges. Our discussion will center primarily on WO_3 and the distortive modes shown in Fig. 2. These distortive modes, all oriented along and around an O–B–O bond axis, are a representative but not exhaustive list of those seen in WO_3 and other d^0 perovskite oxides. These modes can frequently be accessed and tuned by changing temperatures and/or growing thin films biaxially strained by differently sized substrates in the 001 direction. Importantly, our findings for WO_3 can therefore often be generalized to other d^0 perovskite oxides and distortive modes.

C. Effects of distortion on band gaps and edges

The effects of structural distortion on the DFT-LDA-computed band gaps and band-edge energies of WO_3 are summarized in Fig. 3. Band gaps are shown in Fig. 3(a), while the energies of the band-edge orbitals of cubic WO_3 are traced through the lower-symmetry phases in Fig. 3(b). Computed band gaps for each WO_3 phase are compared across density functionals in Table I, demonstrating that the same trends are observed regardless of computational method. Before looking more deeply at why individual distortions have the effects they do, several points are worth noting. First, all of these distortions break the threefold degeneracies at the band edges of cubic WO_3, making the orbitals lying in the 001 planes energetically distinct from those lying in the 100 and 010 planes. Second, distortions tend to cause band edges to move farther apart in energy (if they move at all) due to new orbital mixings that accompany lower symmetry. Third, combining two distortive modes—one in which B-site cations shift and another in which B–O octahedra rotate—leads to a much more significant widening of the band gap than the sum of the individual distortions. For the remainder of this paper, we aim to understand each of these key points.

TABLE I. Computed band gaps of geometrically optimized phases of WO_3, along with their space groups (as determined using the software FINDSYM [65]).

WO_3 phase (Space group)	LDA gap (eV)	PBE gap (eV)	HSE06 gap (eV)
Cubic ($Pm\bar{3}m$)	0.50	0.59	1.62
FE 001 ($P4mm$)	0.52	0.61	1.67
AFE 001 ($P4nmm$)	0.49	0.58	1.65
$a^0a^0c^+$ ($P4/mbm$)	0.51	0.59	1.62
$a^0a^0c^-$ ($I4/mcm$)	0.66	0.66	1.69
FE 001/$a^0a^0c^-$ ($I4cm$)	0.94	0.78	1.86
AFE 001/$a^0a^0c^-$ ($P4/ncc$)	0.98	0.90	2.00

We begin by examining ferroelectric [Fig. 2(a)] and antiferroelectric [Fig. 2(b)] phases in which each B-site cation shifts in the 001 direction (along with small movements of the oxide anions), toward one particular oxide neighbor. As indicated in Fig. 3, both of these distortions break the threefold degeneracies of the cubic band-edge orbitals by making those that lie in the 001 planes distinct from those that lie in the 100 and 010 planes. While the 100- and 010-oriented orbitals move significantly apart in energy, the 001-oriented orbitals remain much the same as those in the cubic structure, leaving the band gaps essentially unchanged. This phenomenon is rationalized in the qualitative orbital pictures in Fig. 4. In cubic WO_3 (or any d^0 perovskite), the band-edge orbitals [Fig. 1(a)] allow no mixing between B-site d states and oxygen $2p$ states. When a B-site cation shifts within its octahedron toward one oxide anion (Fig. 4), the band-edge orbitals lying in the 001 planes remain unmixed, while those lying in the 100 and 010 planes have new mixings between B-site d states and oxide $2p$ states that push their energies apart. Still, because the band gap is defined as the energy difference between the highest filled orbital and lowest unfilled orbital, the lack of mixing in the 001-oriented orbitals leaves the gap nearly unchanged from cubic in the ferroelectric and antiferroelectric structures.

In the case of WO_3, the relaxed ferroelectric and antiferroelectric phases have computed gaps within 0.02 eV of that of the cubic phase. Indeed, for all d^0 perovskites with A = Sr, Ba, Na, and K (which all have tolerance factors between 0.94 and 1.09, making them most likely to exhibit these classes of distortions), the band gaps of the relaxed ferroelectric and antiferroelectric phases are always within 0.07 eV of the corresponding cubic band gap.

We next turn to the other class of perovskite distortions, the rotations of B–O octahedra. As shown in Fig. 3, the $a^0a^0c^+$

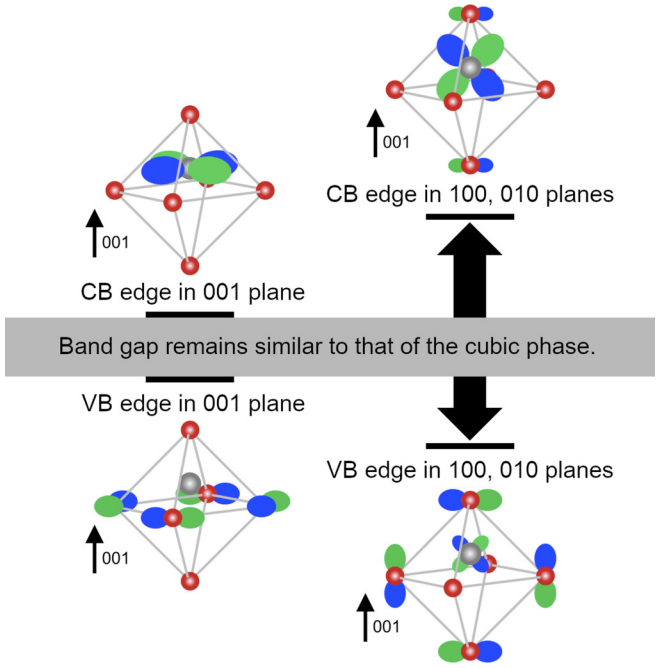

FIG. 4. Schematic illustration of why ferroelectric or antiferroelectric distortions along an O–B–O bond axis of a d^0 perovskite do not lead to significant changes in band gap. When the symmetry is lowered from cubic, band-edge orbitals lying in the 100 and 010 planes (right) are pushed farther apart in the energy, but those lying in the 001 planes (left) retain much the same character as in the cubic phase.

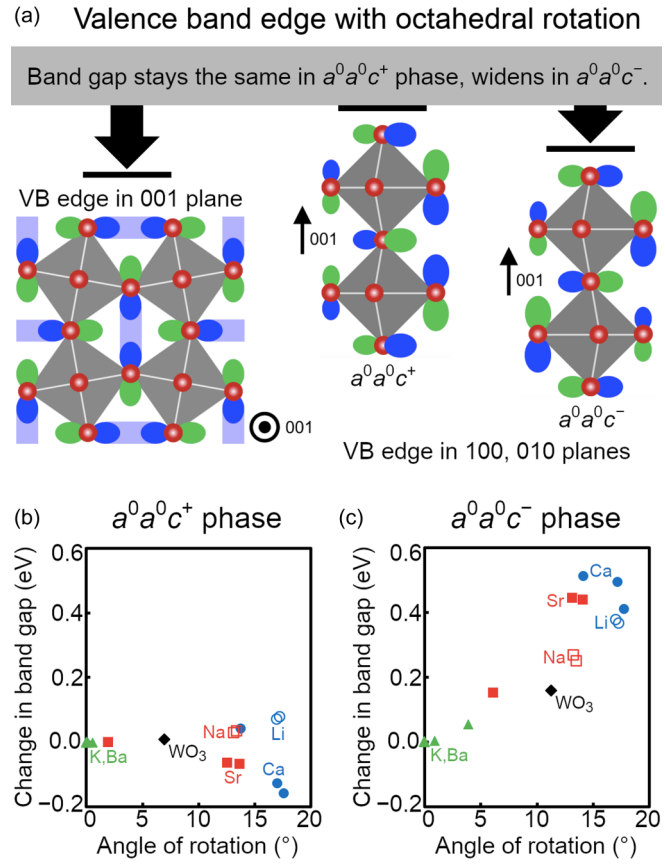

FIG. 5. (a) Schematic illustration of the effect of B–O octahedral rotations on the band gap and band-edge orbitals of WO_3. The extent to which octahedral rotations widen the band gaps of d^0 perovskites is plotted as a function of the angle of rotation for the (b) $a^0a^0c^+$ and (c) $a^0a^0c^-$ phases, grouped by the identity of the A-site element.

distortive mode has little effect on the band gap, widening it by 0.01 eV in WO_3 relative to the cubic phase. The effect of $a^0a^0c^-$ distortion is more significant, widening the band gap of WO_3 by 0.16 eV. These observations can be understood based on the qualitative orbital pictures in Fig. 5(a). When octahedral rotations around a perovskite axis (either $a^0a^0c^+$ or $a^0a^0c^-$) occur, the valence band edge orbital in the 001 planes distorts, enhancing the bonding interactions highlighted on the left side of Fig. 5(a) and lowering the energy of this orbital. The effect of rotation on valence band edge orbitals in the 100 and 010 planes is more subtle. For $a^0a^0c^+$ distortion [Fig. 5(a), center], the energy of these orbitals changes very little, as the antibonding network of oxide $2p$ orbitals remains intact. For $a^0a^0c^-$ distortion [Fig. 5(a), right], the energy of these orbitals shifts downward slightly, as the antibonding network of oxide $2p$ orbitals is broken up when consecutive planes rotate in opposite directions. Though we do not show it in Fig. 5(a), the effects of these distortions on the conduction band edge essentially mirror those on the valence band edge, with orbitals in the 100 and 010 planes staying at the same energy for $a^0a^0c^+$ distortion and shifting upward in energy for $a^0a^0c^-$ distortion.

Putting all of this information together, the band gap of cubic WO_3 remains unchanged by the introduction of $a^0a^0c^+$ rotations, but increases somewhat with the introduction of $a^0a^0c^-$ rotations. Figures 5(b) and 5(c), which plot the change in band gap with the introduction of octahedral rotations (i.e., $a^0a^0c^+$ or $a^0a^0c^-$ band gap minus cubic band gap) as a function of octahedral rotation angle, show that this observation holds for the entire family of d^0 perovskites. When $a^0a^0c^+$ distortions are fully relaxed, the band gap changes by less than 0.16 eV from cubic for all compounds computed. When $a^0a^0c^-$ distortions are fully relaxed, the band gap changes by as much as 0.51 eV. Furthermore, Fig. 5(c) illustrates that the change in band gap is largely an effect of the amplitude of the geometric distortion (driven by the relative sizes of the ions), with larger angles of rotation leading to larger changes in band gap.

D. Effects of combined distortions

Having explored the mechanisms by which individual distortive modes tune WO_3 and perovskite band gaps and band edges, we are now in a position to understand the somewhat surprising effects of *combinations* of distortive modes. Table II shows the computed band gaps of a larger set of WO_3 phases than Table I, including ferroelectric and antiferroelectric distortions, octahedral rotations, and combinations thereof, oriented in various crystallographic directions. It is clear that a combination of distortive modes not only widens the band gap of WO_3, but widens it by much more than the sum of its constituent distortive modes. For example, ferroelectric distortion along 001 widens the band gap of WO_3 by 0.02 eV relative to the cubic phase, $a^0a^0c^+$ octahedral rotation

TABLE II. Computed DFT-LDA band gaps of geometrically optimized phases of WO_3, along with the orientation(s) of the band-edge orbitals whose energies are pushed apart in these distortions. Band gaps widen significantly if and only if the energies of band-edge orbitals in *all three* planes are pushed apart.

WO_3 phase (Space group)	Which band-edge states are affected?	LDA gap (eV)
Cubic ($Pm\bar{3}m$)	None	0.50
FE 001 ($P4mm$)	100, 010	0.52
AFE 001 ($P4nmm$)	100, 010	0.49
FE 110 ($Amm2$)	All	1.04
FE 111 ($R3m$)	All	1.38
$a^0a^0c^+$ ($P4/mbm$)	001	0.51
$a^0a^0c^-$ ($I4/mcm$)	001	0.66
$a^-a^-c^0$ ($Imma$)	100, 010	0.66
$a^-a^-a^-$ ($R\bar{3}c$)	All	0.97
FE 001/$a^0a^0c^+$ ($P4bm$)	All	0.87
AFE 001/$a^0a^0c^+$ ($P42_12$)	All	0.89
FE 001/$a^0a^0c^-$ ($I4cm$)	All	0.94
AFE 001/$a^0a^0c^-$ ($P4/ncc$)	All	0.98

around 001 widens the gap by 0.01 eV, and the combination of these modes widens the gap by 0.37 eV. These "combined distortions" need not consist of an (anti)ferroelectric distortion and an octahedral rotation. Rather, they may consist of one type of distortion in a direction other than 001. For example, ferroelectric distortions in the 110 and 111 directions, which are essentially combinations of distortions along 100, 010, and 001, cause the band gap to increase many times more than distortion along 001. Experimentally in WO_3, lowering the temperature induces phase transitions with additional degrees of small-amplitude octahedral tilting, which further widen the band gap. These phase transitions lower the symmetry from $P4/ncc$ (computed gap = 0.98 eV) to $Pbcn$ (computed gap = 1.20 eV) to $P2_1/n$ (computed gap = 1.20 eV).

This observation that combining distortive modes leads to significant widening of the band gap can be rationalized by recalling how individual distortive modes affect band-edge orbitals. As shown in Figs. 4 and 5, individual distortive modes tend to push apart the energies of only some band-edge orbitals, leading to relatively small changes in band gap. For example, (anti)ferroelectric distortion along 001 only affects band-edge orbitals oriented in the 100 and 010 planes, while octahedral rotation around 001 mainly affects band-edge orbitals oriented in the 001 planes. Therefore, combining these two types of distortion pushes *all* band-edge orbitals (i.e., those oriented in all three planes) apart in energy, widening the gap much more. For each phase of WO_3, Table II shows which band-edge orbitals are affected by distortion. For all phases in which only *some* band-edge orbitals are affected by distortion, the band gap increases by no more than 0.16 eV. For all phases in which *all* band-edge orbitals are affected by distortion, the band gap increases by at least 0.37 eV.

This effect is further illustrated in Fig. 6, in which $a^0a^0c^-$ octahedral rotations of increasing amplitude are frozen into WO_3 in the absence and presence of (anti)ferroelectric distortions. (Anti)ferroelectric distortions themselves have virtually no effect on the band gap of cubic WO_3. However, in the presence of the ferroelectric distortion seen in the $I4cm$ phase or the antiferroelectric distortion seen in the $P4/ncc$ phase, octahedral rotations have a much larger effect on the band gap than they do in isolation.

Another implication of our results, also visible in Fig. 6, is that if one can tune the amplitudes of distortive modes,

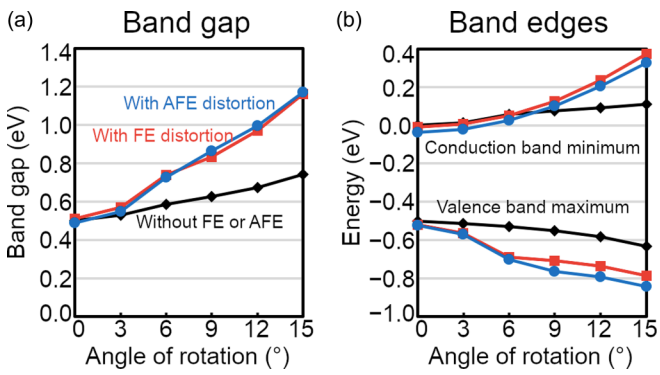

FIG. 6. (a) Band gaps and (b) band-edge energies of WO_3 as $a^0a^0c^-$ octahedral rotations are frozen into the structure, without (black diamonds) and with the presence of the ferroelectric distortions seen in the $I4cm$ phase (red squares) or the antiferroelectric distortions seen in the $P4/ncc$ phase (blue circles).

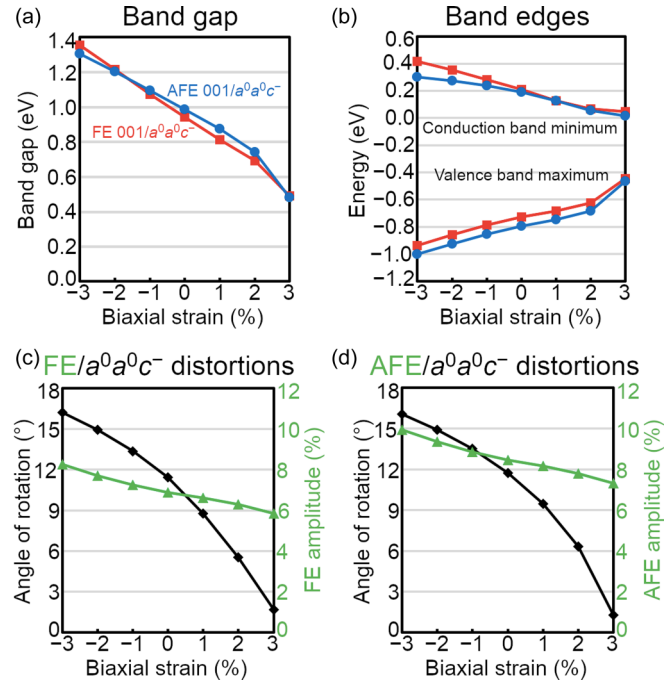

FIG. 7. (a) Band gaps and (b) band-edge energies of the $I4cm$ (red squares) and $P4/ncc$ (blue circles) phases of WO_3, with biaxial strain ranging from −3% (compressive) to +3% (tensile) relative to the fully relaxed structures. (c,d) The amplitudes of both $a^0a^0c^-$ octahedral rotations (black diamonds) and (anti)ferroelectric distortions (green triangles, expressed as a percentage of movement of tungsten toward an oxide anion) are larger under compressive strain, leading to significant tunability of band gaps and edges.

one can tune band gaps and band-edge energies. This can be done in part through the choice of elements, as compounds with tolerance factors farther from $t = 1$ tend to be more distorted than those with tolerance factors close to $t = 1$. Distortive amplitudes can also be tuned by the growth of epitaxially strained thin films. In general, when compressive strain is applied perpendicular to the 001 perovskite axis, a compound adopts (anti)ferroelectric distortions along the 001 axis and/or octahedral rotations around the 001 axis to counteract the shortening of B–O bonds caused by the strain. These effects are demonstrated in Fig. 7, in which the $I4cm$ and $P4/ncc$ phases of WO_3, which combine (anti)ferroelectric distortion and octahedral rotation, are strained perpendicular to the 001 axis from -3% (compressive) to $+3\%$ (tensile). In both phases, compressive strain leads to the widening of band gaps [Fig. 7(a)] and the separation of band edges [Fig. 7(b)], which can be traced to the increase in distortive amplitudes of both the (anti)ferroelectric and $a^0a^0c^-$ modes [Figs. 7(c) and 7(d)]. These behaviors in strained WO_3 are similar to those described in the literature for strained $SrTiO_3$ [19,63].

IV. CONCLUSION

The results in this paper rationalize a few key ideas about the tunability of the band structures and band gaps of WO_3 and d^0 perovskite oxides for photocatalysis. A major weakness of d^0 perovskite oxides as light absorbers for photocatalysis is that their valence band edges are lower in energy than necessary to drive reactions such as water splitting, and their correspondingly large band gaps limit absorption in the solar spectrum. As this work illustrates how and why combinations of distortions lower the valence band edge further, it also suggests that suppressing distortions (via choices of elements, biaxial strains, and elevated temperatures) is generally a route toward raising the valence band edge and reducing the band gap. In the specific case of WO_3, water-splitting photocatalysis is limited by the fact that its conduction band edge is too low in energy to facilitate hydrogen evolution. Therefore, for WO_3, enhancing distortions via compressive strain may be a productive route toward raising the conduction band edge of WO_3 to thermodynamically facilitate water splitting.

Because the trends and qualitative rationale in this paper are based on crystal orbital symmetry and character, our findings are general for both WO_3 and d^0 perovskite oxides. However, WO_3 is somewhat unique among this class because it has a wide variety of phases that include both the shifting of B-site cations and B–O octahedral rotations, which (along with compositional tuning at the tungsten and oxygen sites and cation intercalation at the A site) provide particularly exciting opportunities for electronic tunability.

ACKNOWLEDGMENTS

We gratefully acknowledge the Research Corporation for Science Advancement for financial support through a Cottrell Scholar Award.

[1] M. S. Wrighton, A. B. Ellis, P. T. Wolczanski, D. L. Morse, H. B. Abrahamson, and D. S. Ginley, J. Am. Chem. Soc. **98**, 2774 (1976).
[2] J. G. Mavroides, J. A. Kafalas, and D. F. Kolesar, Appl. Phys. Lett. **28**, 241 (1976).
[3] A. Kudo and Y. Miseki, Chem. Soc. Rev. **38**, 253 (2009).
[4] P. Kanhere and Z. Chen, Molecules **19**, 19995 (2014).
[5] G. Zhang, G. Liu, L. Wang, and J. T. S. Irvine, Chem. Soc. Rev. **45**, 5951 (2016).
[6] E. Grabowska, Appl. Catal. B Environ. **186**, 97 (2016).
[7] R. Shi, G. I. N. Waterhouse, and T. Zhang, Sol. RRL **1**, 1700126 (2017).
[8] W.-J. Yin, B. Weng, J. Ge, Q. Sun, Z. Li, and Y. Yan, Energy Environ. Sci. **12**, 442 (2019).
[9] M. Cardona, Phys. Rev. **140**, A651 (1965).
[10] R. E. Cohen, Nature **358**, 136 (1992).
[11] P. M. Woodward, Acta Cryst. B **53**, 32 (1997).
[12] D. G. Schlom, L.-Q. Chen, C.-B. Eom, K. M. Rabe, S. K. Streiffer, and J.-M. Triscone, Annu. Rev. Mater. Res. **37**, 589 (2007).
[13] J. Hwang, Z. Feng, N. Charles, X. R. Wang, D. Lee, K. A. Stoerzinger, S. Muy, R. R. Rao, D. Lee, R. Jacobs, D. Morgan, and Y. Shao-Horn, Mater. Today **31**, 100 (2019).
[14] C.-H. Lee, N. J. Podraza, Y. Zhu, R. F. Berger, S. Shen, M. Sestak, R. W. Collins, L. F. Kourkoutis, J. A. Mundy, H. Wang, Q. Mao, X. Xi, L. J. Brillson, J. B. Neaton, D. A. Muller, and D. G. Schlom, Appl. Phys. Lett. **102**, 122901 (2013).
[15] S. Vasala and M. Karppinen, Prog. Solid State Chem. **43**, 1 (2015).
[16] D. J. Keeble, S. Wicklein, R. Dittmann, L. Ravelli, R. A. Mackie, and W. Egger, Phys. Rev. Lett. **105**, 226102 (2010).
[17] H. Tan, Z. Zhao, W.-B. Zhu, E. N. Coker, B. Li, M. Zheng, W. You, H. Fan, and Z. Sun, ACS Appl. Mater. Interfaces **6**, 19184 (2014).
[18] H. W. Eng, P. W. Barnes, B. M. Auer, and P. M. Woodward, J. Solid State Chem. **175**, 94 (2003).
[19] R. F. Berger, C. J. Fennie, and J. B. Neaton, Phys. Rev. Lett. **107**, 146804 (2011).
[20] T. Qi, I. Grinberg, and A. M. Rappe, Phys. Rev. B **83**, 224108 (2011).
[21] F. Wang, I. Grinberg, and A. M. Rappe, Appl. Phys. Lett. **104**, 152903 (2014).
[22] E. Salje and K. Viswanathan, Acta Cryst. A **31**, 356 (1975).
[23] K. R. Locherer, I. P. Swainson, and E. K. H. Salje, J. Phys. Condens. Matter **11**, 4143 (1999).
[24] T. Vogt, P. M. Woodward, and B. A. Hunter, J. Solid State Chem. **144**, 209 (1999).
[25] C. J. Howard, V. Luca, and K. S. Knight, J. Phys. Condens. Matter **14**, 377 (2002).
[26] M. E. Straumanis, J. Am. Chem. Soc. **71**, 679 (1949).
[27] M. E. Straumanis and A. Dravnieks, J. Am. Chem. Soc. **71**, 683 (1949).
[28] B. W. Brown and E. Banks, J. Am. Chem. Soc. **76**, 963 (1954).
[29] J. A. Seabold and K.-S. Choi, Chem. Mater. **23**, 1105 (2011).

[30] M. Ma, K. Zhang, P. Li, M. S. Jung, M. J. Jeong, and J. H. Park, Angew. Chem. **128**, 11998 (2016).
[31] S. Hilliard, G. Baldinozzi, D. Friedrich, S. Kressman, H. Strub, V. Artero, and C. Laberty-Robert, Sustain. Energy Fuels **1**, 145 (2017).
[32] J. Huang, P. Yue, L. Wang, H. She, and Q. Wang, Chinese J. Catal. **40**, 1408 (2019).
[33] P. P. González-Borrero, F. Sato, A. N. Medina, M. L. Baesso, A. C. Bento, G. Baldissera, C. Persson, G. A. Niklasson, C. G. Granqvist, and A. F. da Silva, Appl. Phys. Lett. **96**, 061909 (2010).
[34] M. C. Rao and O. M. Hussain, Res. J. Chem. Sci. **1**, 76 (2011).
[35] A. Subrahmanyam and A. Karuppasamy, Sol. Energy Mater. Sol. Cells **91**, 266 (2007).
[36] R. S. Vemuri, M. H. Engelhard, and C. V. Ramana, ACS Appl. Mater. Interfaces **4**, 1371 (2012).
[37] M. B. Johansson, B. Baldissera, I. Valyukh, C. Persson, H. Arwin, G. A. Niklasson, and L. Österlund, J. Phys. Condens. Matter **25**, 205502 (2013).
[38] Y. Ping, D. Rocca, and G. Galli, Phys. Rev. B **87**, 165203 (2013).
[39] F. Wang, C. DiValentin, and G. Pacchioni, J. Phys. Chem. C **115**, 8345 (2011).
[40] H. Hamdi, E. K. H. Salje, P. Ghosez, and E. Bousquet, Phys. Rev. B **94**, 245124 (2016).
[41] S. Z. Karazhanov, Y. Zhang, A. Mascarenhas, S. Deb, and L.-W. Wang, Solid State Ion. **165**, 43 (2003).
[42] D. B. Migas, V. L. Shaposhnikov, V. N. Rodin, and V. E. Borisenko, J. Appl. Phys. **108**, 093713 (2010).
[43] F. Wang, C. DiValentin, and G. Pacchioni, Phys. Rev. B **84**, 073103 (2011).
[44] F. Wang, C. DiValentin, and G. Pacchioni, J. Phys. Chem. C **116**, 8901 (2012).
[45] A. Hjelm, C. G. Granqvist, and J. M. Wills, Phys. Rev. B **54**, 2436 (1996).
[46] A. D. Walkingshaw, N. A. Spaldin, and E. Artacho, Phys. Rev. B **70**, 165110 (2004).
[47] B. Ingham, S. C. Hendy, S. V. Chong, and J. L. Tallon, Phys. Rev. B **72**, 075109 (2005).
[48] S. Tosoni, C. DiValentin, and G. Pacchioni, J. Phys. Chem. C **118**, 3000 (2014).
[49] F. Cora, A. Patel, N. M. Harrison, R. Dovesi, and C. R. A. Catlow, J. Am. Chem. Soc. **118**, 12174 (1996).
[50] G. A. de Wijs, P. K. de Boer, R. A. de Groot, and G. Kresse, Phys. Rev. B **59**, 2684 (1999).
[51] G. Kresse and J. Hafner, Phys. Rev. B **47**, 558 (1993).
[52] G. Kresse and J. Hafner, Phys. Rev. B **49**, 14251 (1994).
[53] G. Kresse and J. Furthmüller, Comput. Mat. Sci. **6**, 15 (1996).
[54] G. Kresse and J. Furthmüller, Phys. Rev. B **54**, 11169 (1996).
[55] G. Kresse and D. Joubert, Phys. Rev. B **59**, 1758 (1999).
[56] J. P. Perdew, K. Burke, and M. Ernzerhof, Phys. Rev. Lett. **77**, 3865 (1996).
[57] A. V. Krukau, O. A. Vydrov, A. F. Izmaylov, and G. E. Scuseria, J. Chem. Phys. **125**, 224106 (2006).
[58] J. B. Neaton and K. M. Rabe, Appl. Phys. Lett. **82**, 1586 (2003).
[59] See Supplemental Material at http://link.aps.org/supplemental/10.1103/PhysRevB.103.045127 for pseudopotential details, structural coordinates, and numerical results corresponding to figures in the body of the paper.
[60] V. M. Goldschmidt, Naturwissenschaften **14**, 477 (1926).
[61] C. J. Bartel, C. Sutton, B. R. Goldsmith, R. Ouyang, C. B. Musgrave, L. M. Ghiringhelli, and M. Scheffler, Sci. Adv. **5**, eaav0693 (2019).
[62] A. M. Glazer, Acta Cryst. B **28**, 3384 (1972).
[63] N. A. Pertsev, A. K. Tagantsev, and N. Setter, Phys. Rev. B **61**, R825 (2000).
[64] K. Momma and F. Izumi, J. Appl. Cryst. **44**, 1272 (2011).
[65] H. T. Stokes and D. M. Hatch, J. Appl. Cryst. **38**, 237 (2005).